

Large scale irregularities in the high latitude F region ionosphere represented by a numerical model, and comparison with Swarm observations

Renata Lukianova^{*,1}

⁽¹⁾ Space Research Institute, Department of Space Plasma, Moscow, Russia

Article history: received October 10, 2025; accepted March 04, 2026

Abstract

A regional numerical model yields a three dimensional electron density distribution in the high latitude F region in the range of 150–600 km. The model takes into account several processes, primarily the plasma convection and auroral particle precipitation, which are crucial for the polar ionosphere. A limited comparison of plasma densities reproduced by the model and obtained from Swarm satellite observations during periods of different IMF orientation is performed. Large scale ionospheric irregularities such as the tongue of ionization and the polar hole, both caused by specific convection patterns, are observed and modeled with sufficient accuracy. When the IMF B_z is positive, a cavity with reduced plasma density is formed in the central polar cap. A tongue of increased ionization extends from the day to the night side across the polar cap, but shifts toward dawn or dusk depending on the sign of the IMF B_y component and, as a consequence, the predominance of a particular convection vortex. Although the polar ionosphere is highly variable and considered poorly modeled, for individual events the physics based model shows reasonable agreement with satellite observations. Results of numerical models can complement and extend the understanding of the high-latitude ionosphere, the morphology of which is simplified in empirical models.

Keywords: High latitude F region ionosphere; Electron density; Numerical modeling; Swarm satellite

1. Introduction

Variability in the electron density in high latitude ionosphere and its dependence on external geophysical conditions, primarily the solar wind and the interplanetary magnetic field (IMF), significantly complicates the modeling of this region. The highest electron concentration occurs in the F region, where the main irregularities form. The maximum N_e is located at an altitude of approximately 250 km in the F2 layer. The ionospheric plasma, in addition to the main ionization by solar extreme ultraviolet (EUV) radiation, is subject to the influence of electrodynamic processes that are controlled by interaction between the magnetosphere and the solar wind. This interaction occurs in the magnetospheric boundary layers, which map onto the high latitude ionosphere. The ionospheric plasma drifts in the crossed geomagnetic and electric fields originated in the outer magnetosphere. Polarization electric fields also appear locally in the ionosphere. Drifting along lines of equal electric potential

through sunlit and dark regions, the ionospheric plasma undergoes greater or lesser ionization. The solar wind energy is stored in the magnetospheric plasma sheet, which is the source of energetic particle precipitation into the high-latitude ionosphere. Precipitation leads to an increased ionization within the auroral oval, especially in the night side. Auroral particles with energies ranging from a few to tens of keV affect the electron concentration at F-layer altitudes both directly and through diffusion processes within the plasma flux tube. The ratio of atomic oxygen (O) and nitrogen (N₂) concentrations in the thermosphere primarily determines the relationship between the formation and loss of charged particles.

The mid-latitude ionosphere is shielded from the solar wind and is considered a relatively quiet and most predictable region. The dominant processes are regular ionization and recombination associated with diurnal variations in solar illumination, as well as tidal movements of the ionized component and neutral gas. Differences between the ionosphere at high and lower latitudes are also due to the fact that the plasma tubes in the inner magnetosphere corotate with the rotating Earth.

Due to high variability of the high-latitude ionosphere, its structure is difficult to predict. The severe weather conditions of the polar region limit the possibilities of monitoring by means of regular ionospheric sounding at a sufficiently large number of observing stations. Compared to mid-latitudes, the number of ionosondes located there is limited. Furthermore, ionograms obtained in polar latitudes are complex, and it can be difficult to interpret them unambiguously. Incoherent scatter radars (ISR) are powerful tools for probing the ionosphere including plasma densities, temperatures, and line-of-sight velocities with high spatiotemporal resolution. Several radar facilities are deployed in the Arctic, some of them are in polar cap (e.g. the EISCAT Svalbard radar, Norway, 75.4° magnetic latitude (MLat) or the RISR-N system located in Resolute Bay, Canada, 82.7° MLat). The radar observations form a valuable dataset of basic ionospheric parameters. However, ESRs do not operate continuously, but rather in relatively short campaigns. Aggregation of data from GPS/GNSS ground-based stations allows for high-resolution total electron content (TEC) maps to be produced. Of the several thousand stations, approximately one-tenth are located at high latitudes. Individual low Earth orbiting (LEO) satellites with suitable orbital inclinations allow in-situ measurements of plasma density in the topside ionosphere.

Meanwhile, there is a need for reliable forecasting of radio communication conditions in polar regions, improving positioning accuracy, and solving other related problems. Various modeling methods are used for these purposes. Based on a specific set of input parameters, primarily solar wind and IMF observations, models attempt to reproduce the three-dimensional (3-D) electron density (N_e) distribution, critical frequency of radio wave reflection in the F2-layer (f_oF2), and TEC. Empirical models are based on the generalization of data from as large as possible number of observations of ionospheric parameters. The most well-known is the International Reference Ionosphere Model (IRI) (Bilitza and Reinisch, 2008; Bilitza et al., 2014; 2017, 2022). At mid-latitudes, IRI provides fairly accurate modeled ionospheric parameters. The heights and peak electron densities of various layers, as well as the TEC values, are in good agreement with experiments, as has been repeatedly confirmed by independent testing (e.g. Arian et al., 2019; Kumar et al., 2025; Okoh et al., 2025).

Empirical models are mainly based on the description of median values of ionospheric parameters for various geophysical conditions. At mid-latitudes, the critical frequencies of the E and F layers undergo regular diurnal and seasonal variations, and the model includes corresponding expressions that approximate these variations. For the high-latitude ionosphere, where transport and precipitation processes predominate, given the significant lack of available observational data, empirical models only provide a background distribution of parameters on spatial scales greater than 1000 km, but do not account for the formation of a large number of irregularities in the F-layer. Describing the near-pole region appears to be a particularly challenging task. Statistical estimates of the IRI accuracy in the high-latitudes were conducted using the ionosonde observations (Themens et al., 2014). Under certain conditions (winter, night-time), differences in maximum electron density parameter $NmF2$ reach tens of percent. This is likely due to the model's underestimation of transport processes, which play a much more significant role in F-layer dynamics at high latitudes compared to low and mid-latitudes, where most of the IRI calibration was conducted. Smaller differences are observed in illuminated daytime summer ionosphere.

The Empirical Canadian High Arctic Ionospheric Model (E-CHAIM) has been developed (Themens et al., 2017). This model is built on the same principles as IRI, but is based on statistics obtained from Arctic and sub-Arctic ionosondes. Of these, only a few stations are located above 65° magnetic latitude (MLat), and even fewer are located above 70° MLat. Meanwhile, E-CHAIM is able to provide a more structured picture than IRI, in particular the wall of the main ionospheric trough (MIT) and the polar cavity can be identified, whereas in IRI they are not modeled (Themens et al., 2020).

Another class of models represents physics-based method. Theoretical models of the high-latitude ionosphere are more flexible, capable of providing a detailed, physically substantiated picture, and allow for various types of “computational experiments” to study the influence of changes in a particular input parameter on the resulting structure of the F-layer (Sojka, 1989; Shunk, 1988; Sojka and Schunk, 1997). Initially, the role of two-cell convection in the ionospheric plasma distribution at high-latitude was demonstrated. The signatures were then associated with the multi-cell convection pattern (Sojka and Shunk, 1987). It was concluded that plasma convection, which is strongly controlled by the orientation of the IMF, is the key factor responsible for large scale ionospheric irregularities. However, the accuracy of reproducing ionospheric irregularities by such models critically depends on the balance of the model components, the completeness of accounting for physical and chemical processes and the coefficients using in the equations.

In this paper, to reproduce the detailed 3-D plasma density distribution above 60° MLat, a numerical model is used, specified for the high-latitude F-region ionosphere, taking into account the solar wind and geomagnetic conditions. The output from the numerical model can complement and expand the representation of the high-latitude part of the ionosphere, the morphology of which is simplified in empirical models such as IRI. For representative geophysical conditions, the simulated N_e distribution is compared with observations from LEO polar-orbiting Swarm satellite at a fixed altitude. Large-scale irregularities in terms of the F-layer peak electron density ($NmF2$) are reproduced giving evidence that the polar upper ionosphere responds strongly to the change in the IMF and solar zenith angle.

2. Modeling approach

Theoretical models for the high-latitude F-layer mathematically formalize three main processes occurring in weakly ionized ionospheric plasma: formation of ions (due to solar radiation and charged particle precipitation), ion losses (due to recombination), and plasma transport, primarily a drift perpendicular to the geomagnetic field lines under the influence of electromagnetic forces. Neutral winds, which produce a dynamo-electric field, also contribute to the plasma motion, but their role is less significant at high latitudes during non-storm times. Ionospheric plasma, ‘frozen’ in a convecting quasi-vertical magnetic flux tube, can travel over long distances through sunlit and dark ionosphere, cross the auroral oval of enhanced precipitation, and stagnate in a specific local time sector if the velocity of electromagnetic drift is compensated by the corotation velocity. The vertical distribution of plasma density depends on the time the tube has spent under certain conditions.

A critical aspect is the adequate specification of the electric potential distribution over the ionospheric shell, that is, the convection trajectories along which the flux tubes drift. The general dependence of convection patterns on the IMF has been formalized in convection models parameterized by the IMF and solar zenith angle. Convection patterns can be obtained from the statistical empirical models (Weimer, 2005; Heppner and Maynard, 1987) or from the SuperDARN observational model (Thomas and Shepherd, 2018). The structure of equipotential contours can also be calculated based on the distribution of field-aligned currents (Lukianova and Christiansen, 2006).

Energies and fluxes of auroral particle precipitation are summarized in a model which is parameterized by the Kp index (Hardy et al., 1987). This model, developed quite a long time ago based on DMSP satellite observations, is nevertheless quite accurate and remains relevant for specification of particle precipitation. There is also a more recent model developed using different satellite data (Zhang and Paxton, 2008). For the thermosphere, the temperature and density of the neutral gas as a function of altitude, geographic location, solar and magnetic activity are given by the empirical model of the MSIS family (Picone et al., 2002), and the neutral wind is given by the empirical model of the HWM family (Hedin et al., 1991; Drob et al., 2008).

The concept of modeling the polar ionosphere, which involves solving the vertical transport equations within a flux tube filled with ionospheric plasma during its convection in crossed electric (E) and magnetic fields (B), was first proposed in (Knudsen et al., 1977). In the Lagrangian approximation, plasma tube convects as a whole, and the condition of vertical continuity should be applied. This condition is satisfied in the F-layer, where ion motion is determined by the $E \times B$ drift. The convection trajectories coincide with the isolines of the ionospheric electric potential.

Soon after the formulation of Knudsen’s approach, regional models based on it were developed (Schunk, 1988; Sojka, 1989; Sojka and Schunk, 1997). These models were mathematically sophisticated and allowed numerical experiments to be performed to identify the influence of each input parameter on the appearance of large-scale ionospheric irregularities. In particular, a time-dependent 3-D model of the middle and high latitude ionosphere

described in (Schunk, 1988) follows flux tubes of plasma as they convect or corotate through a moving neutral atmosphere and accounted field-aligned diffusion, cross-field electrodynamic drifts, thermospheric winds, polar wind escape, energy-dependent chemical reactions, neutral composition changes, ion production due to solar EUV radiation and auroral precipitation, thermal conditions, diffusion-thermal heat flow and local heating and cooling processes. The density distributions of six ion species and the electron and ion temperatures are obtained from a numerical solution of the appropriate continuity, momentum and energy equations.

Despite the need to track the detailed structure of the polar ionosphere, for some reasons (perhaps, the mathematical complexity and inherent uncertainty of parameterization are among them) this class of models did not become particularly popular. It is believed that the high variability of the high-latitude F-layer is generally not amenable to reliable modeling. However, since the number of continuously operating ionospheric observation facilities in the polar region is still limited and the statistical base is not very large, it is of interest to continue developing models of this type and to compare their results with available observational data.

3. Model

An example of a regional numerical model is the Polar F-region Ionosphere Model (PFIM) (Uvarov and Lukianova, 2015; Lukianova et al., 2017). The model is based on the approach proposed by Knudsen (1977). PFIM calculates the distribution of Ne at 150-600 km heights poleward of 50° MLat (CGM) in the approximation of ‘open’ vertical plasma tubes drifting under the influence of the magnetospheric electric field. The input parameters include the day of the year (DOY) and the universal time (UT_{INPUT}), for which the distribution of Ne is calculated, the magnitude IMF B_z and B_y components, the solar wind speed, the f10.7 solar index, and the Kp geomagnetic index. The output is the Ne values at the nodes of a 3-D grid covering the high-latitude region. Based on the obtained data, additional parameters can be calculated, in particular, the 2-D distribution of $NmF2$.

The algorithm for implementing the model consists of two blocks. First, the distribution of electric potential for given IMF and solar wind conditions is modeled. Second, the non-stationary equations describing the change in vertical distribution of ions confined in each unit flux tube, while it drifts along the equipotential line, are integrated. Typically, a 2-D grid with a resolution of 1° in magnetic colatitude (θ), 7.5° in magnetic longitude (φ) is used when calculating the convection pattern. Numerical solution of continuity equations for ions is performed with a height resolution of 10 km and the time step of 10 minutes. The instantaneous distribution of Ne depends on the history of ionization-recombination processes in plasma tubes during their previous movement through the areas of different illumination, precipitation and thermospheric conditions. The initial vertical profile of Ne at each grid point corresponds to a starting instant UT_0 that is sufficiently distant in time (by a few hours) back from the instant UT_{INPUT} . The relaxation time ($UT_{INPUT} - UT_0$) is also specified in the set of input parameters.

Determination of the ionospheric electric potential (U) distribution is based on a schematic analytical representation of field-aligned currents (FAC). The FAC distribution is approximated by a combination of sin and cos functions parameterized with IMF strength and direction. Three separate current systems, R1, R2, and R0 (according to the terminology introduced in (Iijima and Potemra, 1976) are included. The R1 and R2 FACs are associated with the IMF $B_z \leq 0$ conditions, and the R0 FAC is associated with the IMF $B_z > 0$ and with positive or negative polarity of the azimuthal (B_y) component of the IMF.

The equations for closing the magnetosphere-ionosphere current system and Ohm’s law in the ionosphere have the following form:

$$\text{div } \mathbf{J} = j, \quad \mathbf{J} = \sigma \cdot (\text{grad } U), \quad (1)$$

where j is FAC, \mathbf{J} and σ is the height-integrated ionospheric current and conductivity, respectively.

The resulting distributions of U represent the convection patterns with 2, 3 or 4 cells of different intensity. The motion of a plasma tube along an equipotential line, including convection and corotation (the neutral wind dynamo electric field is neglected), is described by equations

$$\frac{\partial \theta}{\partial t} = -2 \cdot E_\varphi(\theta, \varphi) \cdot \frac{(R^2/M) \cdot \cos \theta}{3 \cdot \cos \theta + 1}; \quad E_\varphi = \frac{1}{\sin \theta} \cdot \frac{\partial U}{\partial \varphi} \quad (2)$$

$$\frac{\partial \varphi}{\partial t} = E_{\theta}(\theta, \varphi) \cdot \frac{(R^2/M)}{2 \cdot \cos \theta \cdot \sin \theta} + \omega; \quad E_{\theta} = -\frac{\partial U}{\partial \theta} \quad (3)$$

where t is time; M , ω and R is the Earth's magnetic moment, angular frequency, and radius $R = R_E + 200$ km, respectively.

After completing the first block of the model, which allows one to determine the isocontours of the electric potential, the trajectories and velocity of the drifting tubes, the starting position (θ_0, φ_0) is established for each tube. These coordinates are obtained by tracing each grid point from its actual position to the position it would be at UT_0 (i.e., back in time).

The second block of the model describes the processes of production and loss of ions in each plasma tube as the tube moves along its trajectory during a period from UT_0 to UT_{INPUT} . The vertical integration is performed of the continuity equation for the atomic oxygen ion O^+ (the major species in the F-region) and the non-stationary photochemical equilibrium equation for a generalized ion M^+ :

$$\frac{\partial}{\partial t} n(O^+) = \frac{\partial}{\partial z} \left(D \cdot \frac{\partial}{\partial z} n(O^+) + C \cdot n(O^+) \right) + Q_{O^+} - L_{O^+} \quad (4)$$

$$Q_{M^+} + L_{M^+} = \alpha \cdot n(M^+) \cdot [n(M^+) + n(O^+)] \quad (5)$$

where n is the ion concentration; t is time, z is altitude, the coefficients D and C correspond to the vertical velocity of O^+ , which depends on the ion production rate, thermospheric parameters, collision frequencies, geographic coordinates, and electric and magnetic fields; Q and L is the ionization and ion loss rate, respectively; α is the effective recombination coefficient.

The ion M^+ with an effective mass of 30 a.e.m. represents the N_2^+ , O_2^+ , NO^+ , and H^+ ions, typical for the F-layer. This is a simplification of the chemical composition that speeds up the calculation. The formation of M^+ ions occurs under the influence of solar radiation and precipitation, as well as in the reaction with O^+ . The rates of ionization are calculated using empirical formulas and statistical models. The ion production due to auroral particle precipitation is parameterized based on the statistical model by Hardy et al. (1985, 1987), which provides the average energy, number and energy fluxes of the precipitating auroral particles in the energy spectrum from 50 eV to 20 keV. The primary zone of precipitation due to their energization in the plasma sheet and pitch-angle scattering from the outer radiation belt, is the auroral oval. The contribution of soft electron precipitation on the dayside is also taken into account, in accordance with Hardy's parameterizations. In the thermosphere, the rate of photoionization and ion loss is proportional to the concentration of O and N_2 , respectively. Some of chemical reactions governing the recombination rate are temperature-dependent. The number density and temperature of the neutral thermospheric particles is specified using the MSIS model. At the lower altitude boundary, $n(O^+)$ is determined by the photochemical equilibrium.

4. Modeled plasma density and comparison with IRI at the low-latitude boundary

Empirical models, primarily the IRI standard, reproduce the parameters of the mid-latitude ionosphere up to the subauroral region with great accuracy. For calibration purposes, the PFIM output at the lower latitude boundary is compared with the IRI prediction at the same latitude using a statistical approach. At subauroral latitudes, the main factor determining the value of Ne is the seasonal and diurnal variations of the solar zenith angle. Diurnal variation leads to minimum (maximum) illumination at about 5 (17) UT in the northern hemisphere. Figure 1 shows the simulated $NmF2$ distribution for UT = 5 (Fig. 1a) and UT = 17 (Fig. 1b) at the equinox under zero IMF conditions, slow solar wind $V_{sw} = 350$ km/s, and solar index $f10.7 < 70$ sfu. At 17 UT, due to a larger sunlit area, the ionosphere is generally denser than at 5 UT.

Large-scale irregularities can be identified on both maps. In particular, at about 80° MLat, in the post-noon sector, between 12 and 15 MLTs, a localized polar peak with elevated plasma densities is formed. A large spot of

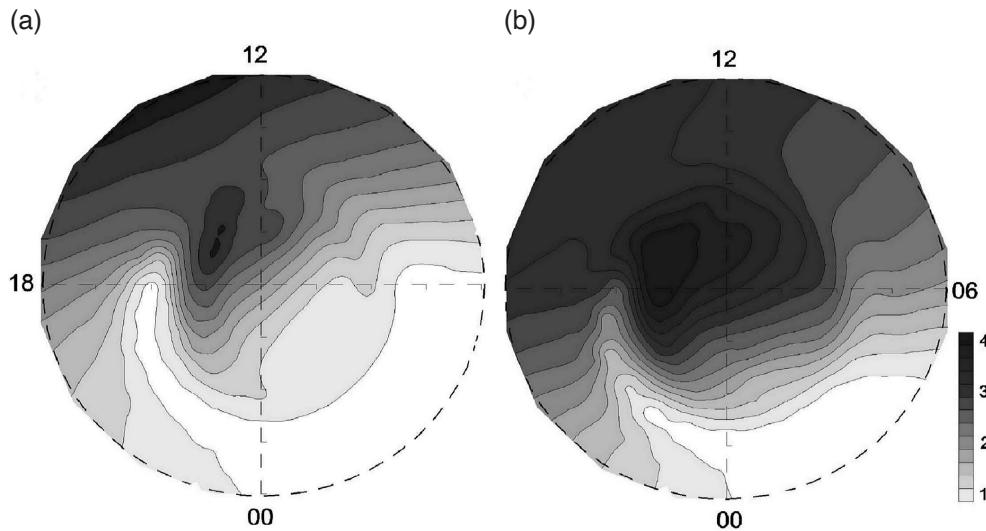


Figure 1. Polar plots of $NmF2$ (10^5 cm^{-3}); northern hemisphere; IMF = 0, Kp = 1; equinox, (a) UT = 05, (b) UT = 17. Each plot is centered at the north magnetic pole; the lower boundary is at 40° colatitude. The white line shows the terminator footprint.

dense plasma is associated with the plasma tubes that have accumulated ionization in the daytime ionosphere. This highly ionized plasma is drawn into the anti-sunward transpolar flow, which is part of a 2-cell convection pattern. From this F-layer peak the plasma density patches often emerge. Besides the convection throat, soft electron precipitation in the cusp region creates a localized, highly turbulent, and intense source of ionization. According to Hardy et al. (1985), in contrast to the nightside auroral precipitation, on the day side, the intensity of number fluxes exhibits little change with Kp.

In the less sunlit ionosphere, in the dawn-midnight sector below $\sim 25^\circ$ colatitudes (75° MLat), the plasma densities become quite low. A notable feature is a low-density channel extending from midnight to dusk, which can be associated with the polar part of the MIT. The depletion arises due to slow drift velocities, stagnation and emptying of plasma tubes in the region of oppositely directed convection and corotation electric fields.

The corotation is taken into account, since it produces a quasi-circumpolar counterclockwise flow at the ionospheric height. When superimposed on a typical 2-cell convection flow, the resulting pattern is dominated by the dawn cell, while the dusk cell is suppressed. Figure 2 shows an example of ionospheric footprint of the trajectories along which flux tubes move under conditions of a purely southward IMF and corotation. In the auroral pre-midnight local sector, the electric fields of convection and rotation are directed oppositely, so the plasma tube velocities there are very low. The main transpolar flow channel shifts from the central polar cap towards the dusk side.

In Fig. 1, a notable feature is the extension of dense plasma from the day- to the night side in the form of a tongue of ionization (ToI). The intensity of ToI depends on the ionization rate and convection velocity. Due to the superposition of convective and corotation electric fields, the ToI tends to shift towards dusk. This corresponds to the structure of the plasma tube trajectories in Fig. 2.

To ensure that the calibration of PFIM is reasonable, the N_e values at the most equatorial latitude available in this model (50° MLat) are compared with the IRI prediction. Under quiet geomagnetic conditions at these relatively low latitudes, ionization by solar ultraviolet radiation is the main factor in plasma production, while convection plays quite a minor role. It is believed that the IRI model correctly describes the mid-latitude ionosphere. Figure 3 shows the paired profiles of $NmF2$ at 50° MLat for 05 UT (Fig. 3a) and 17 UT (Fig. 3b). One of the curves represents the PFIM $NmF2$ values for each solar local time (LT) hour, which are obtained from the maps shown in Fig. 1. Another curve represents the IRI $NmF2$. These values are the averages calculated in the 15-day window centered at the equinoxes (March 21 and September 21) for the years around solar minima (2008-2009, 2019-2020). Further selection is based on the solar wind quietness, when $\sqrt{(B_z^2 + B_y^2)} < 2 \text{ nT}$, $V_{sw} < 350 \text{ km/s}$, and $f_{10.7} < 70 \text{ sfu}$. In total, 13 hours (7 cases at 5 UT and 6 cases at 17 UT) met these conditions. From Fig. 3 it can be seen that the paired variations roughly correspond to each other, with peaks near the afternoon. The displacement of the solar terminator is manifested in the fact that the peak for 05 UT is higher than that for 17 UT. A larger discrepancy

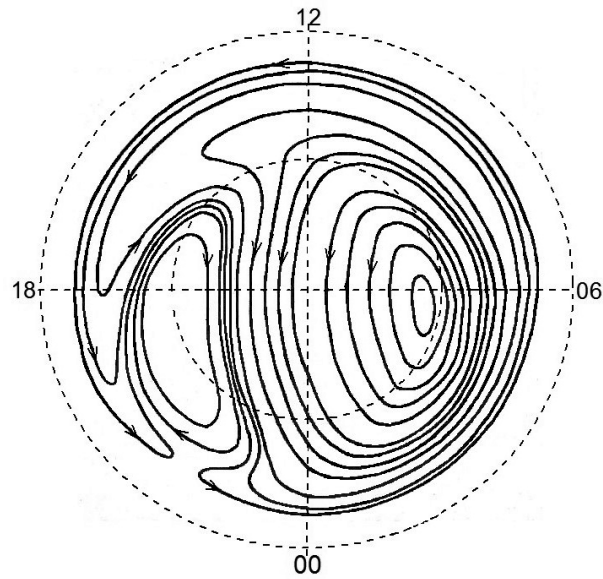


Figure 2. Trajectories of flux tubes for symmetrical two-cell convection and corotation. Arrows indicate the direction of the plasma flow.

between the models is observed in the peak magnitude, when the PFIM maximum is about 20% higher than the IRI peak. However, the parameterization of the PFIM model with respect to solar-induced photoionization appears reasonable since the PFIM results at its low-latitude boundary are generally consistent with IRI predictions.

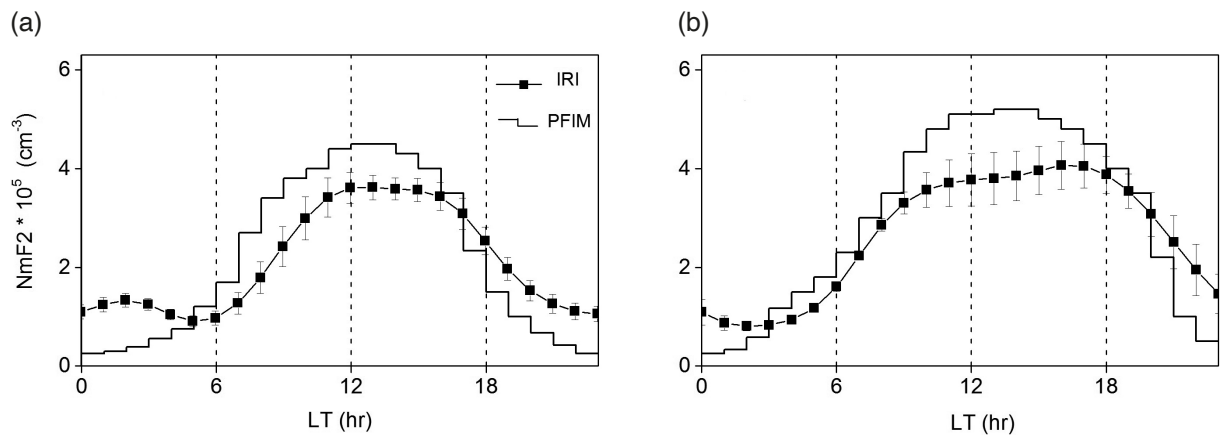


Figure 3. LT-profiles of $NmF2$ at 50° MLat from IRI and PFIM simulations for (a) 05 UT and (b) 17 UT, and nearly zero IMF conditions. A standard deviation is shown for the IRI curves.

5. Observations of large-scale irregularities in the polar ionosphere

To illustrate the ability of the numerical model to reproduce large-scale irregularities, we selected several events of relatively stable IMF and compared the simulated N_e values with Swarm satellite observations at the orbital altitudes. The ESA Swarm constellation consists of three identical satellites (A, B, C) at the polar orbit (Olsen et al., 2013). In 2014, during the initial phase of the mission, Swarm-A and C flew side by side (separated by 1.4° in longitude) at 460 km altitude with an orbital inclination of 87.5° . Swarm-B flies at a higher altitude in a different orbital plane. The satellites make about 15 orbits around the Earth per day. The orbits cover all local time sectors over several months. Over time, the distance between A and C slightly increased and decreased. In 2024, a pair of satellites again

came closest together on parallel trajectories at an altitude of ~ 480 km. Each satellite is equipped with a Langmuir probe (LP) which facilitates the electron density. The 2-Hz plasma data in quasi-dipole (QD) coordinates are available via the online data portal. When the A/C tandem is at a closest distance, their measurements are nearly identical. The data from one satellite (Swarm-A) is used for comparison with the model output. The satellite crosses the high-latitude region in approximately 20 minutes.

With the PFIM model, we simulate the polar ionosphere for a few representative periods during which the satellite orbit was in a plane suitable for crossing large-scale irregularities. In particular, we consider the ToI formed on May 17-19, 2024 and the plasma depletion in the central polar cap, called the polar hole, occurred on June 3, 2014. ToI is a fairly common structure that intensifies during the disturbed periods, while large polar cap area with very low plasma densities represents, in a sense, an anomaly of the quiet ionospheric environment. The selected Swarm-A tracks for both events (three tracks for the ToI event and two tracks for the polar hole event) are shown in Fig. 4. The ToI signature is observed when the satellite passes through the northern polar region along the dawn-dusk meridian. At the time of polar hole formation (labeled as P-hole in Fig. 4) the orbit lies in approximately 21-09 MLT plane.

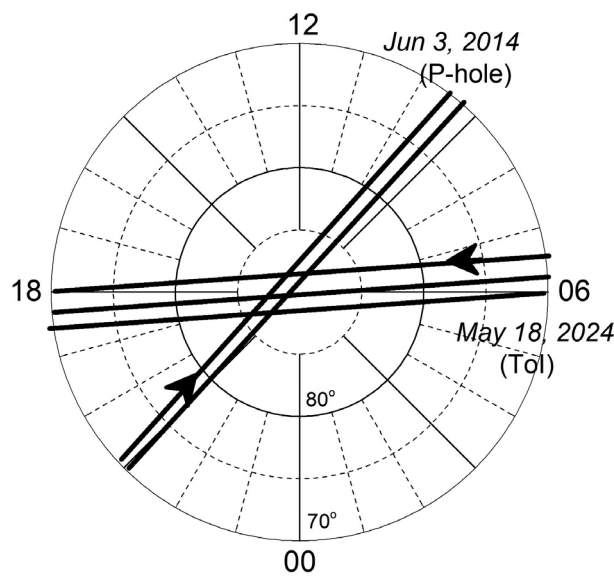


Figure 4. Northern polar view of the selected Swarm-A orbits on June 3, 2014, and May 17-19, 2024; QDLat-MLT coordinates.

6. Evolution of the tongue of ionization

Two-cell convection pattern and the antisunward transpolar flow are responsible for the enhanced ionization expanding from the dayside to the night side through the polar cap, forming ToI. In this section, based on selected events, the formation of ToI under conditions of IMF $B_z \leq 0$ and different signs of B_y is considered. Actual satellite observations are compared with the results of PFIM simulation.

Figure 5 shows the hourly values of IMF B_z , B_y , and the 3-hours K_p index for May 17-19, 2024. At the end of the day on May 17, an increase in geomagnetic activity is observed (K_p up to 6), after which it decreases. At 19 UT, the IMF turns south. Almost simultaneously, the B_y component becomes negative, except a brief excursion to positive at 18 UT. The conditions of $B_z < 0$, $B_y < 0$ remain relatively stable until midday on May 18. After this, the sign of B_y changes to plus, and B_z slowly fluctuates in the range from -5 to $+1$ nT. Three representative UTs were selected for the model simulation. During these periods, the satellite crossed the polar cap ($QDLat > 70^\circ$) at 23:34-23:45 UT, May 17 (event #1), 12:03-12:14 UT, May 18 (event #2), and 17:53-18:02 UT, May 19 (event #3). In Fig. 5, the selected UTs are indicated by colored vertical lines with the corresponding labels. The model input parameters are taken as follows: (#1) DOY = 137 = May 17, UT = 00, $B_z = -8$ nT, $B_y = -7$ nT, $K_p = 5$, $f_{10.7} = 200$; (#2) DOY = 138 = May 18, UT = 12, $B_z = -5$ nT, $B_y = 0$ nT, $K_p = 2$, $f_{10.7} = 200$; (#3) DOY = 139 = May 19, UT = 18, $B_z = -3$ nT, $B_y = +8$ nT, $K_p = 2$, $f_{10.7} = 205$.

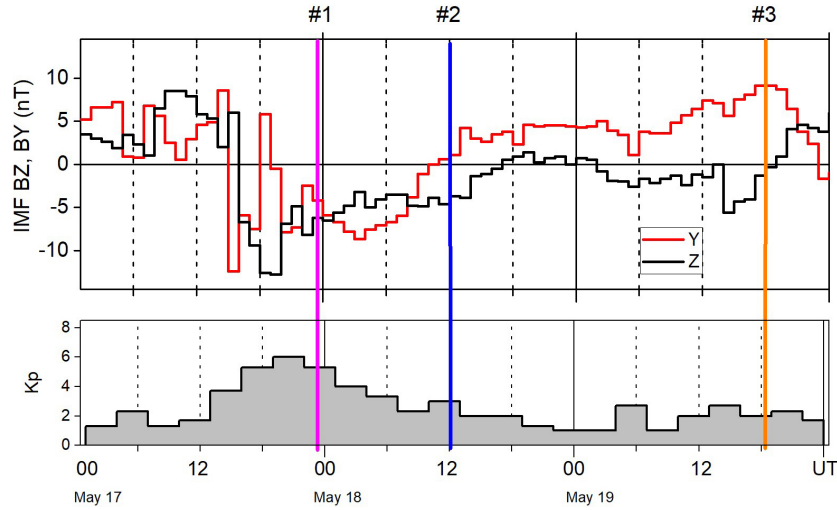


Figure 5. The IMF Bz, By, and Kp index for May 17-19, 2024. Three vertical colored lines mark the time of selected Swarm passes through the polar cap (events #1, #2 and #3). The model simulation is performed for these moments.

Figure 6 shows the polar diagrams of the $NmF2$ distribution for the three events under consideration. In all cases, the IMF is southward. The IMF By turns from minus to zero and to plus. Comparing the panels, one can see substantial changes in the structure of $NmF2$, namely the different location of ToI relative to the noon-midnight meridian. When $By < 0$, a ToI-like signature, a crescent-shaped region of dense plasma, extends from prenoon to dusk and midnight (event #1, Fig. 6a). When $By \approx 0$, at 12 UT on May 18, a similar structure is reproduced, but only on the dusk side (event #2, Fig. 6b). Event #3, at 18 UT on May 19, occurs after a prolonged period of $By > 0$. As a result, the ToI is shifted to the opposite sector between 00 and 11 MLT (Fig. 6c).

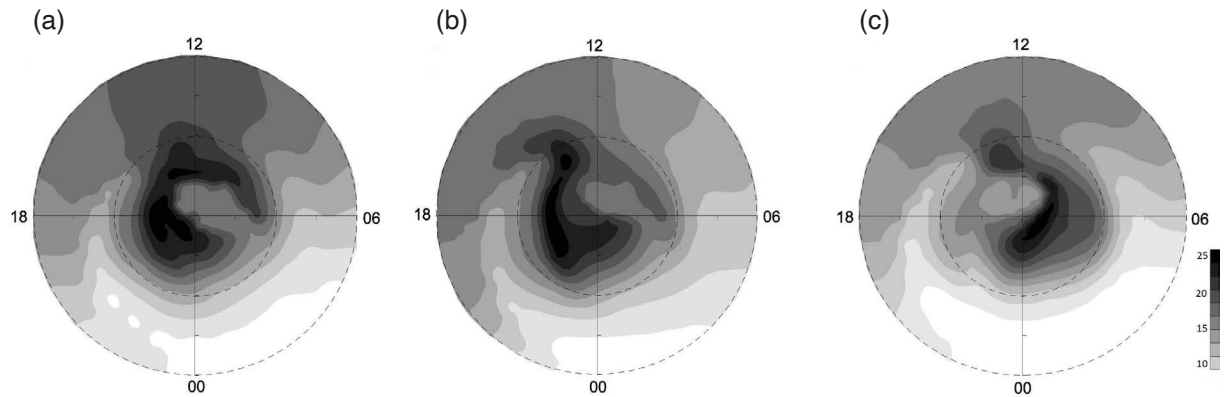


Figure 6. Polar plots of $NmF2$ (10^5 cm^{-3}) distribution simulated for events #1 ($By < 0$), #2 ($By \approx 0$), and #3 ($By > 0$).

In May 2024, the Swarm-A satellite crossed the northern polar cap from dawn to dusk. This trajectory is well suited for detecting ToI, which is expected to manifest itself as an increase in Ne at a specific location. Figure 7 shows the modeling results in comparison with Swarm observations along the orbit. The Ne values were calculated at 480 km altitude and interpolated in the horizontal plane onto a projection of satellite's passage. The raw 2 Hz data from the Swarm LP instrument were averaged over 21 points. Panel (a), (b), (c) shows the calculated and actually observed Ne values for events #1, #2, and #3, respectively. The difference between CGM and QD latitudes is neglected since it is small at polar latitudes. All three plots demonstrate qualitative agreement in the shape of paired curves, although the simulated profiles are, as expected, smoother. When $By < 0$, Swarm-A observes a peak in Ne up to $50 \cdot 10^4 \text{ cm}^{-3}$ at $80\text{--}85^\circ$ QDLat, while on the dawn side the density is considerably lower (Fig. 7a). The model predicts a peak value of $35 \cdot 10^4 \text{ cm}^{-3}$. When By approaches to zero after a prolonged negative period, the ToI continues to be located at dusk,

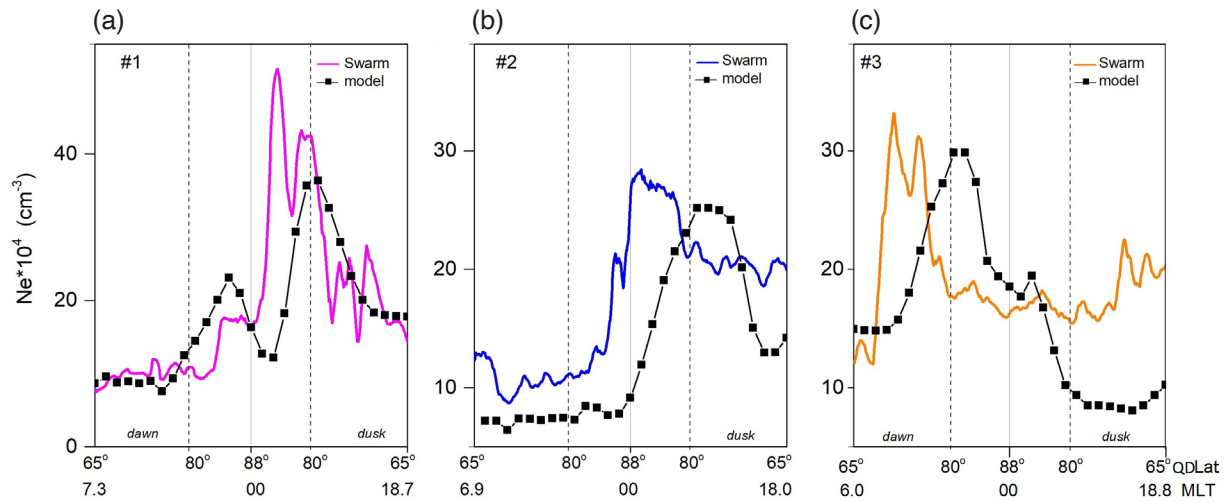


Figure 7. The change in N_e actually observed along the Swarm pass and calculated for the same altitude for (a) event #1, $B_y < 0$, (b) event #2, $B_y \approx 0$, and (c) event #3, $B_y > 0$. The color of the lines representing the Swarm data is similar to the color of the vertical lines marking events in Fig. 5.

and both, the measured and calculated, peaks decrease down to $25 \cdot 10^4 \text{ cm}^{-3}$ (Fig. 7b). When $B_y > 0$, a maximum of about $30 \cdot 10^4 \text{ cm}^{-3}$ is observed on the dawn side (Fig. 7c). The observed and calculated densities are in qualitative agreement. Their complete coincidence is unlikely to be expected.

The ability of the PFIM model to reproduce a realistic ToI position is based on a reasonable parameterization of the convection flow. A convection cell, forming in the pre-noon or post-noon sector, is responsible for the corresponding displacement of ToI. Under conditions of $B_y \neq 0$, a three-cell convection pattern is developed, as schematically illustrated in Fig. 8 for the case of $B_y < 0$. Within the near-noon vortex, plasma flows counterclockwise. With the opposite polarity of B_y , this pattern is mirrored. The near-noon cell often merges with one of the larger vortices of the dominant two-cell pattern. The resulting pattern turns out to be asymmetric relative to the noon-midnight meridian. The electric field increases either on the dawn or on the dusk side. Being under the primarily control of this factor, the ToI shifts towards dawn (dusk) if $B_y > 0$ ($B_y < 0$). The intensity of ToI for $B_y < 0$ is usually greater

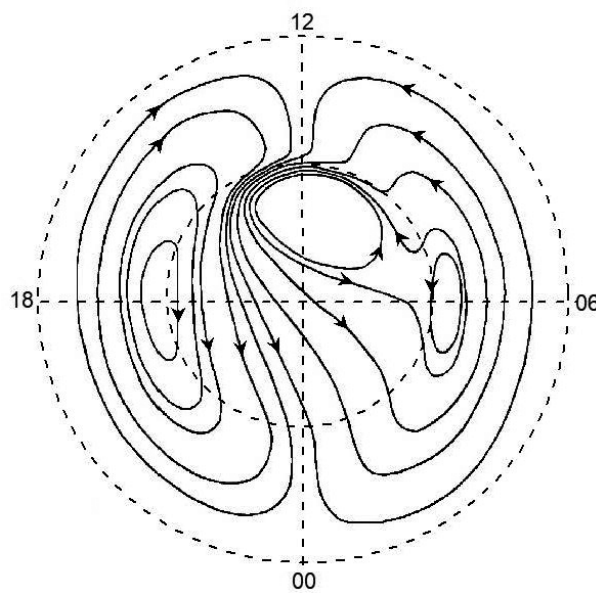


Figure 8. Trajectories of flux tubes for 3-cell convection under conditions of the IMF $B_y < 0$. The effect of corotation is not included.

compared to that for $B_y > 0$. On the dusk side, the ToI merges with the polar peak into a single structure, which, due to the corotation effect, tends to shift more towards dusk.

Returning to Fig. 7, one can notice a systematic bias of $5\text{--}10^\circ$ in the latitudinal position of the simulated and actual observed ToI. If $B_y \leq 0$ (Fig. 7ab), the observed ToI on the dusk side is located closer to the pole than the simulated one. If $B_y > 0$ (Fig. 7c), the model predicts the ToI to occur at $\sim 80^\circ$ QDLat on the dawn side, while the satellite observes the N_e peak at $70\text{--}75^\circ$ QDLat, i.e. further from the pole. Observations imply that the dusk convection cell expands more strongly under the influence of the positive IMF B_y compared to effect of the negative B_y on the dawn cell. In the former case, the transpolar flow associated with ToI is located on the dawn side and at lower latitudes. In the latter case, the flow shifts towards dusk side and passes closer to the pole. This likely is a manifestation of absence of exact mirroring in the convection pattern governing by opposite B_y signs, as mentioned, e.g., in (Ruohoniemi and Greenwald, 2005).

7. Polar hole

The polar holes are believed to be formed during the periods of slow convection, in the absence of ionization sources, during geomagnetic quietness and reduced solar illumination (Sojka et al., 1981). Recent radar observations have shown that such plasma depletions can also occur over a wider range of space weather conditions (Forsythe et al., 2021). Based on the assumption that a hole occurs more frequently when the IMF B_z is northward, representative events were selected to demonstrate the ability of our model to reproduce this ionospheric irregularity. On June 3, 2014 from 03 to 10 UT, relatively stable conditions of $B_z \approx +5$ nT, $B_y \approx -5$ nT were observed. Over the next hours (10–14 UT) the IMF B_y was slightly negative, B_z strengthened up to $+8$ nT, and $K_p \approx 1$ (Fig. 9). The modeling simulation is performed for the input parameters corresponding to 12 UT. This event was preceded by a 10-hour interval of the northward IMF. For comparison with the simulation results, the two closest in time Swarm satellite passes over the northern hemisphere are selected. The satellite crosses the latitudes $>70^\circ$ QDLat at 10:58–11:08 UT and 12:32–12:43 UT (events #4 and #5).

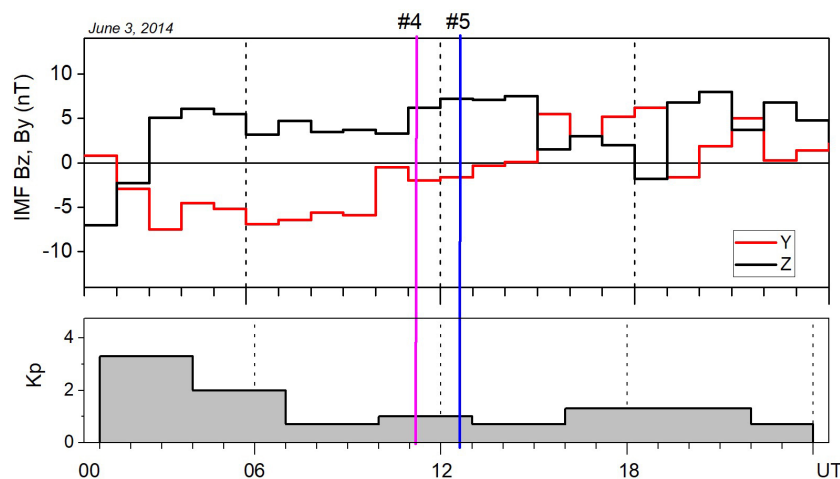


Figure 9. The IMF B_z , B_y , and K_p index for June 3, 2014. Two vertical colored lines mark the time of selected Swarm passes through the northern polar cap.

Figure 10 shows the polar diagram of the modeled $NmF2$ for the IMF conditions corresponding to 12 UT (the time approximately between the satellite passes #4 and #5). In this fig., two of the most prominent large-scale anomalies can be identified. The first one is the duskside ToI, which merges with the polar peak and extends slightly onto the dawn side. In the central polar cap, between the two branches of the ToI, a cavity with considerable plasma depletion is revealed. The location and depth of the polar hole are consistent with what would be expected during geomagnetically quiet times, assuming convection is a key factor. If the northward IMF prevails, a four-cell convection pattern is formed. In the additional dayside vortices, the plasma tubes drift in a direction opposite to the

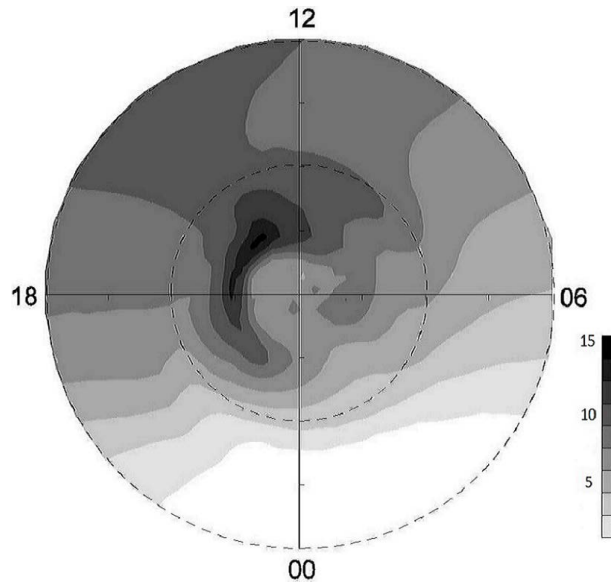


Figure 10. Polar plot of $NmF2$ (10^5 cm^{-3}) distribution simulated for June 3, 12 UT, $B_z = +6 \text{ nT}$, $B_y = -2 \text{ nT}$.

drift in the dawn and dusk vortices. As a result, most tube trajectories deviate from the central polar cap towards its boundary, and a small amount of new dense plasma enters the near-pole area. Photoionization remains the only factor of plasma production. Without a horizontal transport, continuous recombination effectively reduces the electron density even in the summer polar cap.

Figure 11 shows the actually observed and modeled (at the satellite orbital altitude) Ne values along the Swarm-A tracks which cross the northern polar region from dusk to dawn in the meridional plane 21-09 MLT. The satellite observes a pronounced decrease in Ne from about $15 \cdot 10^4$ down to $9 \cdot 10^4 \text{ cm}^{-3}$ (~40%) in the central polar cap. A moderate increase, likely associated with ToI, is observed at approximately 80° QDLat on the dusk side. A similar variation is reproduced in the PFIM simulation. The relative depth of the polar hole (about 30%) is consistent with observations. At the same time, for these particular events, the model predicts considerably smaller absolute values of Ne . The discrepancy may be due to either a general underestimation of Ne or a too rapid decrease with height above the F2 layer maximum.

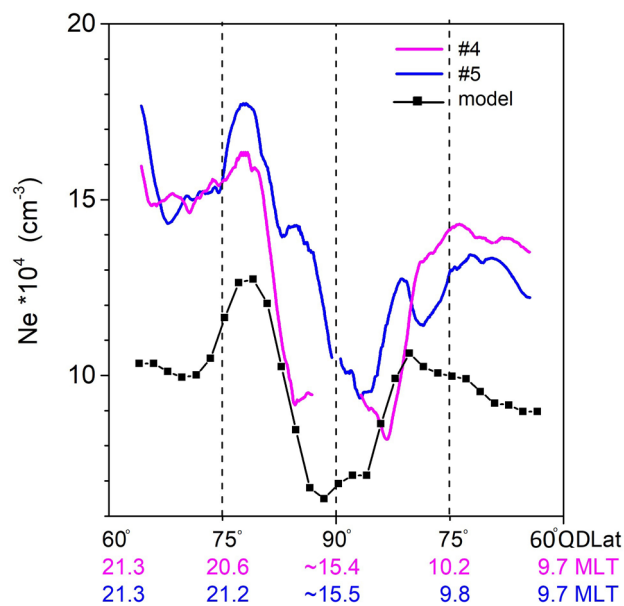


Figure 11. Variations of Ne actually observed along the Swarm passes for events #4 and #5, and those calculated for the same altitude.

A more strict condition at the upper boundary could perhaps reduce the difference. In the modeling approach, the plasma tubes are assumed to be open to the magnetosphere. This implies the possibility of O⁺ outflow. Although the diffusion process primarily involves light ions, O⁺ ions also escape. However, the current version assumes a zero O⁺ concentration at 600 km altitude, partly because of insufficient knowledge of the ion distribution applicable for parameterization. The vertical plasma drift associated with Joule heating of the underlying thermosphere and changes in chemical composition (a decrease in O/N₂) is unlikely to play a significant role if $B_z > 0$ and little energy enter the magnetosphere. Further calibration of the model results above the F2 maximum using satellite data may help to assess the influence of ion outflow.

8. Discussion

The events discussed in sections 6 and 7 were selected for modeling under different IMF conditions and geomagnetic activities, and the results were compared with the Swarm satellite observations. The actually observed and modeled *Ne* variations demonstrate how the high-latitude F region ionospheric irregularities are formed under the influence of the convective transport of the ionospheric plasma driven by magnetospheric electric field. Changes in the IMF direction and strength lead to a considerable reorganization of the basic two-cell convection pattern and displacement of the convection vortices. Besides convection, other factors contribute to the formation of large-scale irregularities, including precipitation, thermospheric conditions and movement of the solar terminator. Various smaller-scale irregularities are constantly present in the polar ionosphere. In particular, electromagnetic and plasma waves, Alfvén turbulence and anomalous heating as feedback from small-scale turbulence play a significant role.

The events under consideration occurred during periods of relatively stable IMF. In most cases the evolution of ionospheric irregularities occurs under the influence of a continuously changing IMF. Therefore, the actual convection trajectories differ from those determined in the quasi-stationary approximation, when the IMF is considered constant during the period between the value UT specified as an input parameter (UT_{INPUT}) and a starting point UT_0 from which the plasma tubes is being traced. The uncertainty introduced by the approximation of the constant convection pattern is small if the IMF has not changed during several hours before the event in question. Theoretically, it is possible to trace individual convection trajectories calculated with a stepwise change of IMF. However, an attempt to practically implement this approach in a computational code showed that individual trajectories often become tangled. A more efficient, although non-physical, approach to obtaining the most realistic electron density distribution is a kind of ensemble calculation. For example, if we assume that the IMF changes every 30 min and the relaxation time interval ($UT_{INPUT} - UT_0$) is at least 4 hours, then we need to run the model 8 times, specifying the corresponding IMF and UT as input parameters. The obtained data sets are then combined with the appropriate weights into the final *Ne* distribution. The closer (in terms of the number of time steps) a particular data set is to the final one, the higher the weighting factor. Testing this approach has shown promising results. However, in this study, we avoided using this methodology because the IMF remained relatively stable across the selected events. Under such “idealized” conditions, the PFIM model appears to be able to reproduce the large-scale irregularities actually observed.

The model based on the governing equations may also be limited by its inherently schematic representation of key parameters, especially the convection patterns. However, with a statistical approach, the simulated distributions of *Ne* are in reasonable qualitative agreement with the experimental data (Lukianova and Bogoutdinov, 2017; Lukianova and Kozlovsky, 2020). Although direct comparison with observations for particular events often proves inconsistent, the case studies presented here are examples of reasonably good model representations of actually observed large-scale ionospheric irregularities.

The simulation results and satellite observations seems consistent with the proposed mechanisms of polar hole formation. The depleted *Ne* can be associated with the convection reversal in the regions of weak convection and prolonged recombination in darkness (Sojka et al., 1991; Benson and Grebowsky, 2001). It typically occurs during low geomagnetic activity, and when the IMF is northward. The low-energy (~100 eV) polar rain electrons are uniformly distributed throughout the polar cap. They are not energized in the plasma sheet, but are directly associated with the solar wind. Polar rain electrons lead to an increase in *Ne*, but primarily at the altitudes below 200 km (Zou et al., 2025). Another possible factor is a vertical movement related to ion frictional heating as the result of relative drift between ions and neutrals due to thermospheric winds (Bjoland et al., 2021). However, the neutral winds were not included

when simulating this event. Therefore this mechanism hardly contributed to the formation of the depletion region, whereas convection remains the main driver.

Convection also transports ionospheric plasma across the dayside cusp and through the polar cap to the night side, forming ToI. The properties of ToI have been extensively studied using the space and ground based observations (e.g. Foster et al., 2005; Thomas et al., 2013; Klimenko et al., 2019). The IMF B_y polarity is crucial for the dawn-dusk asymmetry in the convection pattern and displacement of ToI towards dusk if $B_y < 0$, and towards dawn if $B_y > 0$ (northern hemisphere). This occurs because the transpolar (antisunward) plasma flow becomes more intense on the corresponding side of the polar cap boundary (Lukianova and Kozlovsky, 2011). When the IMF B_y changes sign from minus to plus on May 17-19, the Swarm satellite, passing through the northern high-latitude region in the 06-18 MLT plane, observes ToI on the dusk and dawn side, respectively. In this case, the model demonstrates its ability to accurately reproduce the occurrence of ToI associated with IMF polarity, as well as reasonable agreement with observations. It should be noted that large-scale plasma structures are transported from the dayside to the polar cap, often modified by localized precipitation. Convective mixing of this precipitated plasma with background density gradients contribute to F-layer smaller-scale irregularities. The high geomagnetic activity is favorable for further extension of the ToI-like structures from the noon sector to the dawn and dusk sides.

9. Conclusion

The PFIM numerical model yields a 3-D electron density distribution in the high-latitude F region in the range of 150-600 km. The model is considered regional because it involves several factors, primarily the plasma convection and particle precipitation, which are not need to be taken into account at mid-latitudes but are crucial for the polar ionosphere. We performed a limited comparison of electron densities predicted by the model and derived from Swarm satellite observations during periods of different IMF orientation. The large-scale ionospheric irregularities such as a tongue of ionization and a polar hole, both caused by specific convection pattern are well observed and modeled with a sufficient accuracy. When the IMF B_z is positive, a cavity with reduced N_e values ($\sim 7 \cdot 10^4 \text{ cm}^{-3}$ at the Swarm altitude) is formed in the central polar cap. A tongue of increased ionization extends from the day to the night side across the polar cap, shifting toward dawn or dusk depending on the sign of the IMF B_y component and the predominance of a particular convective vortex. The actual extension can be estimated with some uncertainty because the satellite crossed the polar cap along the dawn-dusk meridian, and because the model may not have adequately accounted for the impact of auroral particle precipitation.

Although the polar ionosphere is highly variable and is considered poorly modeled, for selected events the physics-based model shows reasonable agreement with satellite observations. The output of this class of models can complement and extend the understanding of the high-latitude part of the ionosphere, the morphology of which is simplified in empirical models.

Data availability statement. The Swarm LP dataset are publically accessible via <https://swarm-diss.eo.esa.int/>. The IMF and Kp index are available via the NASA OMNI database (<https://omniweb.gsfc.nasa.gov/>). The IRI model is available via the Community Coordinated Modeling Center (<https://ccmc.gsfc.nasa.gov/models/IRI~2016/>). The GNU Fortran has been used for building the software package for the PFIM numerical model.

Acknowledgements. The author acknowledges discussions within the International Space Science Institute (ISSI) Team 23-580 "Meteors and Phenomena at the Boundary between Earth's Atmosphere and Outer Space" and the ISSI Visiting Scientist Program.

References

- Arikan, F., U. Sezen and T. L. Gulyaeva (2019). Comparison of IRI-2016 F2 layer model parameters with ionosonde measurements, *J. Geophys. Res.*, 124, 10, 8092-8109, doi:10.1029/2019JA027048.
- Benson, R. F. and J. M. Grebowsky (2001). Extremely low ionospheric peak altitudes in the polar hole region, *Radio Sci.*, 36, 2, 277-285, doi:10.1029/1999RS002401.

- Bilitza, D. and B. W. Reinisch (2008). International Reference Ionosphere 2007: Improvements and new parameters, *Adv. Space Res.*, 42, 4, 599-609, doi:10.1016/j.asr.2007.07.048.
- Bilitza, D., D. Altadill, Y. Zhang, C. Mertens et al. (2014). The International Reference Ionosphere 2012 – a model of international collaboration, *J. Space Weather Space Clim.*, 4, A07, doi:10.1051/swsc/2014004.
- Bilitza, D., D. Altadill, V. Truhlik, V. Shubin et al. (2017). International Reference Ionosphere 2016: From ionospheric climate to real-time weather predictions, *Space Weather*, 15, 2, 418-429, doi:10.1002/2016SW001593.
- Bilitza, D., M. Pezzopane, V. Truhlik, D. Altadill et al. (2022). The International Reference Ionosphere model: A review and description of an ionospheric benchmark, *Rev. Geophys.*, 60, 4, e2022RG000792, doi:10.1029/2022RG000792.
- Bjoland, L. M., Y. Ogawa, U. P. Løvhaug, D. A. Lorentzen et al. (2021). Electron density depletion region observed in the polar cap ionosphere, *J. Geophys. Res. Space Phys.*, 126, 1, e2020JA028432, doi:10.1029/2020JA028432.
- Drob, D. P., T. Emmert, G. Crowley, J. M. Picone et al. (2008). An empirical model of the Earth's horizontal wind fields: HWM07, *J. Geophys. Res.*, 113, A12, 304, doi:10.1029/2008JA013668.
- Foster, J. C., A. J. Coster, P. J. Erickson, J. M. Holt et al. (2005). Multiradar observations of the polar tongue of ionization, *J. Geophys. Res.*, 110, A9, A09S31, doi:10.1029/2004JA010928.
- Forsythe, V. V., B. Kunduri and S. Zou (2021). Multi-instrument investigation of the polar holes, *J. Geophys. Res.*, 126, 12, e2021JA029795, doi:10.1029/2021JA029795.
- Hardy, D. A., M. S. Gussenhoven and E. Holeman (1985). A statistical model of auroral electron precipitation, *J. Geophys. Res.*, 90, A5, 4229-4248, doi:10.1029/JA090iA05p04229.
- Hardy, D. A., M. S. Gussenhoven, R. Raistrick and W. J. McNeil (1987). Statistical and functional representations of the pattern of auroral energy flux, number flux, and conductivity, *J. Geophys. Res.*, 92, A11, 12275-12294, doi:10.1029/JA092iA11p12275.
- Hedin, A. E., M. A. Biondi, R. G. Burnside, G. Hernandez et al. (1991). Revised global model of thermospheric winds using satellite and ground based observations, *J. Geophys. Res.*, 96, A5, 7657-7688, doi:10.1029/91JA00251.
- Heppner, J. P. and N. C. Maynard (1987). Empirical high-latitude electric field model, *J. Geophys. Res.*, 92, A5, 4467-4489, doi:10.1029/JA092iA05p04467.
- Iijima, T. and T. A. Potemra (1976). The amplitude distribution of field-aligned currents of northern high latitudes observed by Triad, *J. Geophys. Res.*, 81, 13, 2165-2174, doi:10.1029/JA081i013p02165.
- Klimenko, M. V., I. E. Zakharenkova, V. V. Klimenko, R. Y. Lukianova et al. (2019). Simulation and observations of the polar tongue of ionization at different heights during the 2015 St. Patrick's Day storm, *Space Weather*, 17, 1073-1089, doi:10.1029/2018SW002143.
- Knudsen, W. C., P. M. Banks, J. D. Winningham and D. M. Klumpar (1977). Numerical model of the convecting F2 ionosphere at high latitudes, *J. Geophys. Res.*, 82, 29, 4784-4792, doi:10.1029/JA082i029p04784.
- Kumar, V. V., R. A. Marshall, A. E. Chand, T.-W. Fang et al. (2025). On the performance of ionospheric models in estimating foF2, *Space Weather*, 23, 9, e2025SW004330, doi:10.1029/2025SW004330.
- Lukianova, R. Y. and F. Christiansen (2006). Modeling of the global distribution of ionospheric electric field based on realistic maps of field-aligned currents, *J. Geophys. Res.*, 111, A3, A03213, doi:10.1029/2005JA011465.
- Lukianova, R., V. M. Uvarov and P. Coisson (2017). High-latitude F region large-scale ionospheric irregularities under different solar wind and zenith angle conditions, *Adv. Space Res.*, 59, 2, 557-570, doi:10.1016/j.asr.2016.10.010.
- Lukianova, R. and A. Kozlovsky (2020). Electron density in the polar F region ionosphere during solar minimum: Modeling, radar and ionosonde observations, *Russ. J. Earth Sci.*, 20, ES1004, doi:10.2205/2019ES000699.
- Lukianova, R. and Sh. Bogoutdinov (2017). Large-scale irregularities of the winter polar topside ionosphere according to data from Swarm satellites, *Cosmic Res.*, 55, 436-445, doi:10.1134/S0010952517060077.
- Lukianova, R. and A. Kozlovsky (2011). IMF By effects in the plasma flow at the polar cap boundary, *Ann. Geophys.*, 29, 7, 1305-1315, doi:10.5194/angeo-29-1305-2011.
- Okoh, D., C. Cesaroni, J. B. Habarulema et al. (2025). Investigation of the global climatologic performance of ionospheric models utilizing in-situ Swarm satellite electron density measurements, *Adv. Space Res.*, 75, 5, 4274-4290, doi:10.1016/j.asr.2024.08.052.
- Olsen, N., E. Friis-Christensen, R. Floberghagen et al. (2013). The SWARM satellite constellation application and research facility (SCARF) and SWARM data products, *Earth Planets Space*, 64, 11, 1189-1200, doi:10.5047/eps.2013.07.001.
- Picone, J. M., A. E. Hedin, D. P. Drob and A. C. Aikin (2002). NRLMSISE-00 empirical model of the atmosphere: Statistical comparisons and scientific issues, *J. Geophys. Res.*, 107, A12, 1468, doi:10.1029/2002JA009430.

- Ruohoniemi, J. M. and R. A. Greenwald (2005). Dependencies of high-latitude plasma convection: Consideration of interplanetary magnetic field, seasonal, and universal time factors in statistical patterns, *J. Geophys. Res.*, 110, A9, A0204, doi:10.1029/2004JA010815.
- Schunk, R. W. (1988). A mathematical model of the middle and high latitude ionosphere, *Pure Appl. Geophys.*, 127, 2-3, 255-303, doi:10.1007/BF00879813.
- Sojka, J. J., W. J. Raitt and R. W. Schunk (1981). A theoretical study of the high-latitude winter F region at solar minimum for low magnetic activity, *J. Geophys. Res.*, 86, 609-621, doi:10.1029/JA086iA02p00609.
- Sojka, J. J. (1989). Global scale physical models of the F region ionosphere, *Rev. Geophys.*, 27, 3, 371-403, doi:10.1029/RG027i003p00371.
- Sojka, J. J. and R. W. Schunk (1987). Theoretical study of the high-latitude ionosphere's response to multicell convection patterns, *J. Geophys. Res.*, 92, A8, 8733-8744, doi:10.1029/JA092iA08p08733.
- Sojka, J. J. and R. W. Schunk (1997). Simulations of high latitude ionospheric climatology, *J. Atmos. Sol. Terr. Phys.*, 59, 2, 207-229, doi:10.1016/S1364-6826(96)00037-5.
- Sojka, J. J., R. W. Schunk, W. R. Hoegy and J. M. Grebowsky (1991). Model and observation comparison of the universal time and IMF By dependence of the ionospheric polar hole, *Adv. Space Res.*, 11, 10, 39-42, doi:10.1016/0273-1177(91)90318-E.
- Themens, D. R., P. T. Jayachandran, M. J. Nicolls and J. W. MacDougall (2014). A top to bottom evaluation of IRI 2007 within the polar cap, *J. Geophys. Res. Space Phys.*, 119, 8, 6689-6703, doi:10.1002/2014JA020052.
- Themens, D. R., P. T. Jayachandran, I. Galkin and C. Hall (2017). The empirical Canadian High Arctic ionospheric model (E-CHAIM): NmF2 and hmF2, *J. Geophys. Res. Space Phys.*, 122, 8, 9015-9031, doi:10.1002/2017JA024398.
- Themens, D. R., P. T. Jayachandran, B. Reid and A. M. McCaffrey (2020). The limits of empirical electron density modeling: Examining the capacity of E-CHAIM and the IRI for modeling intermediate (1-to 30-day) timescales at high latitudes, *Radio Sci.*, 55, 4, e2018RS006763, doi:10.1029/2018RS006763.
- Thomas, E. G., J. B. H. Baker, J. M. Ruohoniemi, L. B. N. Clausen et al. (2013). Direct observations of the role of convection electric field in the formation of a polar tongue of ionization from storm enhanced density, *J. Geophys. Res. Space Phys.*, 118, 3, 1180-1189, doi:10.1002/jgra.50116.
- Thomas, E. G. and S. G. Shepherd (2018). Statistical patterns of ionospheric convection derived from mid-latitude, high-latitude, and polar SuperDARN HF radar observations, *J. Geophys. Res. Space Phys.*, 123, 4, 3196-3216, doi:10.1002/2018JA025280.
- Uvarov, V. M. and R. Yu. Lukianova (2015). Numerical modeling of the polar F region ionosphere taking into account the solar wind conditions, *Adv. Space Res.*, 56, 11, 2563-2574, doi:10.1016/j.asr.2015.10.004.
- Weimer, D. R. (2005). Improved ionospheric electrodynamic models and application to calculating Joule heating rates, *J. Geophys. Res.*, 110, A5, A05306, doi:10.1029/2004JA010884.
- Zhang, Y. and L. J. Paxton (2008). An empirical Kp-dependent global auroral model based on TIMED/GUVI FUV data, *J. Atmos. Sol.-Terr. Phys.*, 70, 8-9, 1231-1242, doi:10.1016/j.jastp.2008.03.008.
- Zhou, S., L. Wang, Z. Wu, Z. Zhou et al. (2025). Modeling of the ionospheric electron density variations induced by intense polar rain electron precipitation, *Adv. Space Res.*, 76, 6, 3681-3691, doi:10.1016/j.asr.2025.07.025.

***CORRESPONDING AUTHOR: Renata LUKIANOVA,**

Space Research Institute, Department of Space Plasma, Moscow, Russia

e-mail: renaluk@gmail.com

© 2026 the Author(s). All rights reserved.

Open Access. This article is licensed under a Creative Commons Attribution 4.0 International